Estimation of absolute stress in the hypocentral region of the 2019 Ridgecrest, California, earthquakes

Y. Fialko[1]

[1]Institute of Geophysics and Planetary Physics, Scripps Institution of Oceanography, University of California, San Diego, La Jolla, California, USA.

Key Points:

- Distribution of dihedral angles between active conjugate faults is used to estimate the magnitude of deviatoric stress at seismogenic depth
- Dihedral angles are quantified using linear clusters of precisely located earthquakes and focal mechanism data
- Data from the Ridgecrest (California) area suggests in situ coefficient of friction of 0.4-0.6, and depth-averaged shear stress of 25-40 MPa

Abstract

Strength of the upper brittle part of the Earth's lithosphere controls deformation styles in tectonically active regions, surface topography, seismicity, and the occurrence of plate tectonics, yet it remains one of the most debated quantities in geophysics. Direct measurements of stresses acting at seismogenic depths are largely lacking. Seismic data (in particular, earthquake focal mechanisms) have been used to infer orientation of the principal stress axes. I show that the focal mechanism data can be combined with information from precise earthquake locations to place constraints not only on the orientation, but also on the magnitude of absolute stress at depth. The proposed method uses relative attitudes of conjugate faults to evaluate the amplitude and spatial heterogeneity of the deviatoric stress and frictional strength in the seismogenic zone. Relative fault orientations (dihedral angles) and sense of slip are determined using quasi-planar clusters of seismicity and their composite focal mechanisms. The observed distribution of dihedral angles between active conjugate faults in the area of Ridgecrest (California, USA) that hosted a recent sequence of strong earthquakes suggests in situ coefficient of friction of 0.4-0.6, and depth-averaged shear stress on the order of 25-40 MPa, intermediate between predictions of the "strong" and "weak" fault theories.

1 Introduction

There is a long-standing debate regarding the level of average shear stress in the Earth's crust (Rice, 1992; Hardebeck & Hauksson, 2001; Scholz, 2000). Estimates of earthquake stress drops place a lower bound on shear stress resolved on seismogenic faults on the order of 1-10 MPa (Choy & Boatwright, 1995; Allmann & Shearer, 2009). Laboratory measurements of quasi-static rock friction (Byerlee, 1978; Dieterich, 1981; Marone, 1998; Mitchell et al., 2013, 2015), orientation of young faults with respect to the inferred principal stress axes (Walsh & Watterson, 1988; Collettini & Sibson, 2001), and measurements in deep boreholes in stable intraplate interiors (Zoback et al., 1993; Townend & Zoback, 2000) suggest that the brittle upper crust should be able to support much higher shear stresses on the order of the lithostatic pressure (> 100 MPa for ~15 km thick seismogenic zone), provided that the pore fluid pressure is approximately hydrostatic. Extrapolation of laboratory measurements of quasi-static friction to in situ rock failure, and the assumption of hydrostatic pore pressure constitute the so-called "strong fault" theory (Byerlee, 1978; Scholz, 2000).

In contrast, unfavorable orientation of some mature faults with respect to the principal stress axes (Mount & Suppe, 1987; Wernicke, 1995; Wang & Fialko, 2018), the "heat flow paradox" of the San Andreas Fault (Lachenbruch & Sass, 1980), high degree of slip localization on exhumed faults (Chester et al., 2005; Fialko, 2015), a possibility of fluid over-pressurization (Sibson, 2004), low frictional strength of some parts of mature faults suggested by scientific drilling experiments (Lockner et al., 2011), and strong dynamic weakening observed in laboratory friction experiments at slip rates in excess of ∼ 0.1 m/s (Han et al., 2007; Di Toro et al., 2011; Goldsby & Tullis, 2011; Brown & Fialko, 2012) lend support to the "weak fault" theory according to which faults may operate at background shear stresses well below the failure envelope predicted by the Byerlee's law (e.g., Sibson, 1990; Noda et al., 2009; Thomas et al., 2014; Collettini et al., 2019). Low effective friction on major plate boundary faults is also warranted by geodynamic models of large-scale tectonic phenomena such as subduction and orogeny (e.g., Toth & Gurnis, 1998; Sobolev & Babeyko, 2005; Stern & Gerya, 2018).

One possible explanation reconciling disparate views on the magnitude of shear stresses in the lithosphere is that the effective fault strength may depend on the fault "age", or total offset: young developing faults may be relatively strong while mature well-slipped faults may be weak, possibly because of activation of various weakening

mechanisms with an increasing cumulative slip (Fialko & Khazan, 2005; Rice, 2006; Noda et al., 2009; Thomas et al., 2014; Fialko, 2015; Collettini et al., 2019). However, conditions that govern such a transition, and the evolution of fault strength as a function of a cumulative offset are still poorly known.

Our understanding of the fault strength problem is severely limited by the lack of measurements of shear stress at seismogenic depths. Apart from a scarce set of point measurements in deep boreholes (Plumb & Hickman, 1985; Zoback et al., 1993; Lockner et al., 2011), most of the available information is derived from analyses of seismic data. The most commonly used method of "stress inversion" relies on earthquake focal mechanisms to solve for the orientations of principal stress axes that are most consistent with all of the focal mechanisms in a specified volume (Gephart & Forsyth, 1984; Michael, 1987; Hardebeck & Hauksson, 2001). This method however is unable to determine the magnitude of shear stress.

In this paper I show that under certain conditions the magnitude of shear stress can be estimated using a distribution of fault orientations with respect to one of the principal stress axes, or between sets of conjugate faults activated by a given ambient stress. One location where the respective conditions appear to be met is the northern part of the Eastern California Shear Zone near the town of Ridgecrest that hosted a sequence of strong earthquakes in 2019 (Ross et al., 2019; Hauksson & Jones, 2020; Jin & Fialko, 2020). I use microseismicity data collected prior to the occurrence of the 2019 earthquake sequence to identify active faults in the Ridgecrest area, quantify their orientations, and use the latter to evaluate the magnitude of shear stress acting in the seismogenic zone.

2 Conjugate faults as stress meters

Laboratory experiments and geological observations indicate that failure of relatively intact rocks is well described by the Mohr-Coulomb theory (Lockner et al., 1992; Walsh & Watterson, 1988; Collettini & Sibson, 2001; Scholz, 2019). The latter predicts that the failure criterion is independent of the intermediate principal stress (i.e., is intrinsically two-dimensional), and failure can equally likely occur on mutually antithetic sets of planes that are parallel to the intermediate principal stress axis, and make an acute angle with the maximum compressive stress axis. The antithetic failure planes are referred to as conjugate faults (Anderson, n.d.; Twiss & Moores, 1992, p. 173). A dihedral angle between the newly formed conjugate faults is a measure of internal friction, and can be used to infer the state of stress at the time of failure (Barton, 1976; Angelier, 1994). In practice, available data rarely allow one to discriminate between slip on newly formed vs pre-existing faults, and/or faults that experienced a finite rotation since their inception (e.g., Nur et al., 1986; Fialko & Jin, 2021). Seismic focal mechanisms that are widely used to infer orientations of the principal stress axes in the seismogenic zone (Gephart & Forsyth, 1984; Michael, 1987; Hardebeck & Hauksson, 2001) are not suitable for studying the relationships between active conjugate faults because of two fundamental limitations. First, uncertainties in the fault plane solutions are typically too large, especially for small to intermediate-size events (Hardebeck & Shearer, 2002; Yang et al., 2012; Duputel et al., 2012), to be useful for evaluation of dihedral angles. Second, an intrinsic ambiguity between the two nodal planes in a focal mechanism does not allow one to isolate sets of synthetic vs antithetic faults, required to define a dihedral angle between the respective fault planes.

These limitations can be mitigated by combining information provided by focal mechanisms with geometric constraints from the well-determined earthquake hypocenters. Precisely relocated seismicity catalogs reveal ubiquitous lineated clusters of earthquakes that illuminate faults or fault segments of various sizes and strikes (e.g., see
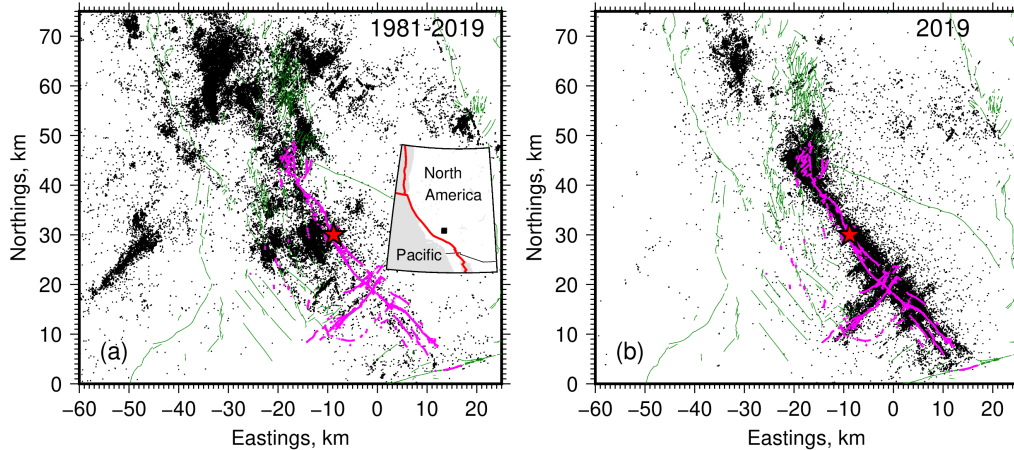
Figure 1. (a) Precisely relocated seismicity in the Ridgecrest-Coso area over a time period 1981-July 2019 (Hauksson et al., 2012). Thin green lines denote Quaternary faults (Jennings & Bryant, 2010). Magenta lines denote surface traces of the 2019 ruptures (DuRoss et al., 2020). Red star denotes the epicenter of the 2019 M7.1 earthquake. Inset shows the location of the study area. (b) Precisely relocated seismicity over 6 months following the July 2019 M7.1 event (Ross et al., 2019). Local origin is at 117.5°W, 35.5°N.

Figure S1 in Supplementary Materials). Such clusters of earthquakes can be used to map the distribution and attitude of active faults throughout the seismogenic layer. Fault strikes can be determined with accuracy up to several degrees, an order of magnitude improvement over the individual focal mechanism solutions. Also, fault orientations (well defined by seismicity lineations) along with the polarity of focal mechanisms uniquely constrain the sense of fault slip. I illustrate the method using data from the Ridgecrest area in the Eastern California Shear Zone (ECSZ) that hosted a sequence of strong earthquakes in 2019 (Figure 1).

3 Data and methods

The ECSZ is an emergent plate boundary that accommodates an increasing fraction of the relative motion between the Pacific and North American plates since its inception 6-10 Ma (Dokka & Travis, 1990; Nur et al., 1993; McClusky et al., 2001; Tymofyeyeva & Fialko, 2015; Floyd et al., 2020). As such, the ECSZ is a natural laboratory for studying the development and evolution of new as well as re-activation of old fault systems. The ECSZ is currently the most seismically active region in California, with 3 major earthquakes occurring over the last 30 years (Sieh et al., 1993; Hauksson et al., 2002; DuRoss et al., 2020). The most recent major event with magnitude 7.1 occurred in July 2019 near the town of Ridgecrest in the northern part of the ECSZ (Figure 1), and involved rupture of a system of right and left-lateral strike-slip faults (Ross et al., 2019; Hauksson & Jones, 2020; Jin & Fialko, 2020).

The nearly perpendicular orientation of conjugate faults ruptured by the Ridgecrest earthquakes (Figure 1b) is distinctly different from optimal orientations predicted by the strong fault theory (dihedral angles of 50-60 degrees for the coefficient of friction of 0.6-0.8) (Sibson, 1990; Scholz, 2019). This prompted suggestions that in situ coefficient of friction is close to zero (Ross et al., 2019). Alternatively, high-angle conjugate faults could result from rotation away from the optimal orientation since the initiation of the ECSZ (Fialko & Jin, 2021). As noted by Fialko and Jin (2021), a pat-

tern of high-angle faulting similar to that involved in the 2019 earthquake sequence is prevalent in a broader region around the 2019 ruptures (Figure 1a). I start by quantifying the distribution of fault strikes and relative orientations between conjugate faults expressed in microseismicity (Figure 1a).

3.1 Analysis of fault orientations

To identify a population of active faults in the Ridgecrest area, I use a refined catalog of earthquake focal mechanisms for southern California with earthquake locations derived from waveform cross-correlation (Yang et al., 2012), updated to include data up to year 2020 (see Data Availability Statement). The catalog data for the area of interest include around 3.2×10^4 focal mechanisms for earthquakes that occurred between January 1981 and July 2019 (Figure 1a). The orientation of seismically active faults is evaluated using the following procedure. Seismicity on sub-vertical strike-slip faults is manifested by lineated clusters of epicenters in the map view (Figure 1). I use an unsupervised learning algorithm OPTICS (Ordering Points To Identify the Clustering Structure) to select clusters of events that satisfy prescribed criteria of proximity and density (Ankerst et al., 1999). An event epicenter is selected as a core point of a cluster if it has a number of geometrically defined neighbors equal to or greater than 10. The search algorithm is executed iteratively, with an increasing distance that defines neighbors within a cluster, from 0.5 to 1.5 km. At the end of each iteration selected clusters are removed from the catalog and the search continues. Clusters chosen by the OPTICS algorithm can have diverse geometries that are not necessarily linear. To select clusters that have a quasi-linear shape, and estimate the best-fit linear trends, I use RANSAC (Random Sample Consensus) (Schnabel et al., 2007) and robust linear regression algorithms. This method is similar to that used by Skoumal et al. (2019) to analyze induced seismicity in central Oklahoma, although the two approaches were developed independently. One advantage of the clustering algorithm used in this study is that it allows for identification of relatively small faults in the neighborhood of large clusters of earthquakes. In addition, I interrogate a three-dimensional (3-D) distribution of earthquake hypocenters to identify quasi-planar surfaces using a robust statistics algorithm for plane detection in unorganized point clouds (Araújo & Oliveira, 2020). To maximize the likelihood of feature detection in three dimensions, I use the full waveform-relocated catalog (Hauksson et al., 2012) which has ∼3 times more events than the focal mechanism catalog (Yang et al., 2012). Planar features that were not associated with a sufficient number of clustered hypocenters in the focal mechanism catalog were excluded from the subsequent analysis. The 3-D plane detection and the 2-D line clustering methods produced a number of spatially overlapping features that likely represented the same fault structures. In such cases only one best-fitting fault segment was retained.

Examples of selected event clusters are shown in Figure 2. For each of the linear fits to the scattered epicenter locations (see red lines and black dots in Figure 2), I estimate errors in the best-fit strike angle by computing deviation of the least-square linear fits treating northing and easting coordinates as independent variables (Fialko, 2004). The respective errors are shown as red numbers for each cluster (see Figure 2). On average the estimated uncertainties in fault strikes are on the order of several degrees.

3.2 Analysis of slip direction

To determine the sense of slip on the identified fault segments, I use focal mechanisms of events in the respective clusters. For each event I compute components of the seismic moment tensor M_{ij} from the magnitude (M_w), strike, dip, and rake angles provided in the focal mechanism catalog, $M_{ij} = M_0(u_i n_j + u_j n_i)$, where $M_0 = 10^{1.5 M_w + 9.1}$ is the scalar seismic moment in newton meters, n_i is the normal to a slip plane (defined
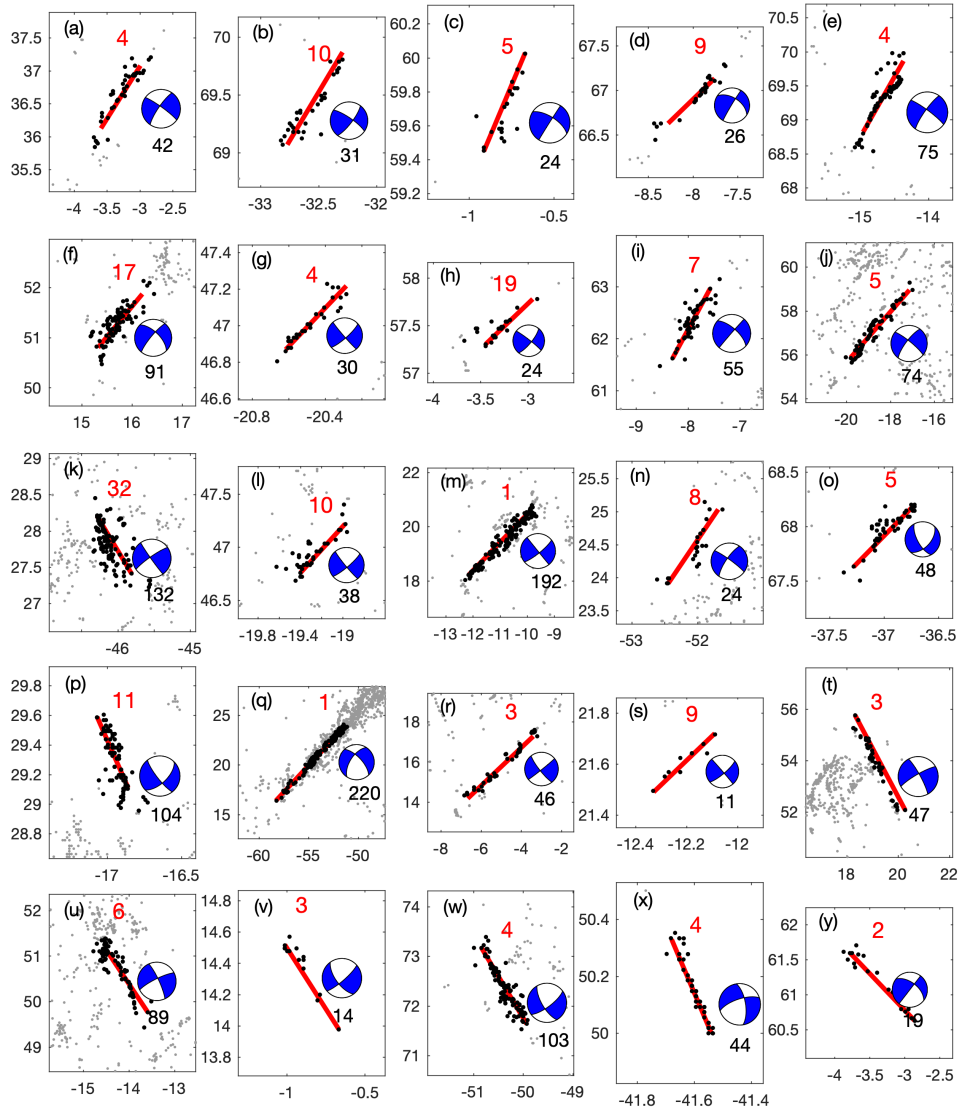
Figure 2. Seismicity lineations identified by the clustering algorithm. Grey dots denote the background seismicity, black dots denote events included in a cluster. The local UTM coordinate system is the same as in Figure 1. Red lines denote the best linear fits. White and blue "beach balls" denote the composite focal mechanisms for the respective clusters. Black numerical labels below the beach balls indicate the number of events in a cluster. Red numerical labels above the beach balls indicate uncertainty in the estimated strike angle, in degrees.
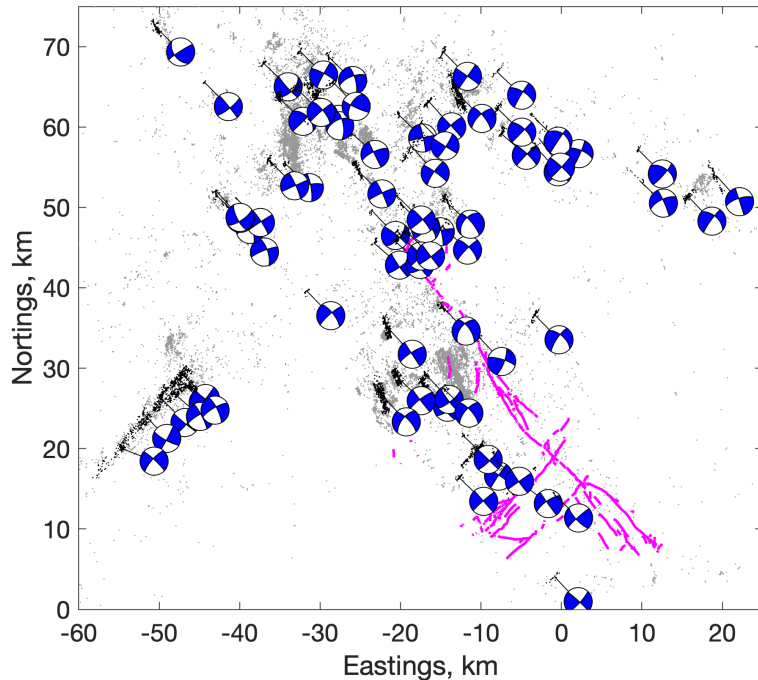
Figure 3. Map of the Ridgecrest-Coso area. Magenta wavy lines denote surface traces of the 2019 ruptures mapped by field surveys (DuRoss et al., 2020). Grey dots denote pre-earthquake (1981-2019) seismicity from the focal mechanism catalog (Yang et al., 2012). Black dots denote seismicity lineations selected by the clustering algorithm (see Supplementary Materials and Figures S2-S4 for details). White and blue "beach balls" denote the best-fitting double-couple composite focal mechanism for the respective linear clusters of earthquakes. Coordinates the same as in Figure 1.

by the strike and dip angles), and u_i is the unit slip vector (defined by n_i and the rake angle). I then compute a tensorial sum $\Sigma_k M_{ij}$, where k is the number of events in a cluster. To investigate the effect of diversity of focal mechanisms (e.g., to avoid a possible dominance of a largest event in a cluster), I also use moment tensors normalized by their scalar moments, $\bar{M}_{ij} = M_{ij}/\sqrt{M_{mn}M_{mn}/2}$ (repeated indices imply summation). I find that using original and normalized moment tensors gives rise to essentially the same results.

The composite moment tensors may have an appreciable non-double-couple component if focal mechanisms of events in a cluster are highly diverse. Yet orientations of the P and T axes (that determine the average sense of slip on a plane defined by a seismicity lineation) are well resolved. The focal mechanisms shown in Figure 2 represent the best-fit double couple solutions for composite moment tensors $\Sigma_k \bar{M}_{ij}$. For some event clusters, the composite focal mechanisms revealed a nearly vertical plunge of the P axis, suggestive of a predominantly dip-slip motion. The respective clusters were removed from the dataset. Application of the algorithm described in this Section to the background (prior to July 2019) seismicity data (Figure 1a) resulted in selection of 70 quasi-linear clusters of micro-earthquakes. The respective clusters are shown in Figure 3, and individually in Figures 2 and S1-S2. The composite focal mechanisms of the identified clusters are predominantly strike-slip, with approximately north-south
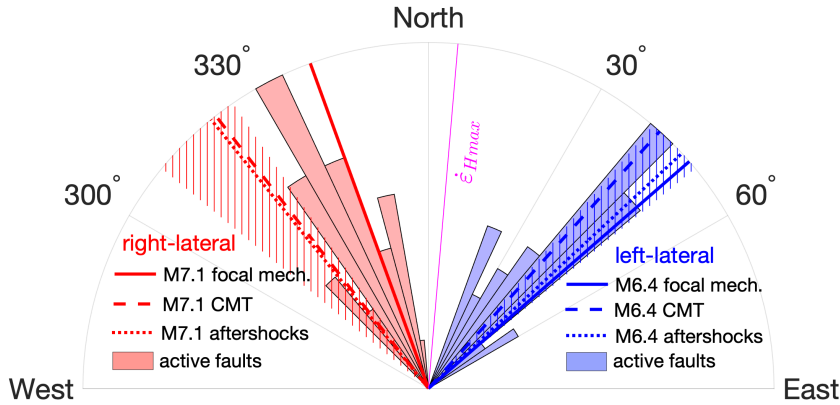
Figure 4. A distribution of strikes of 70 active fault segments shown in Figure 3. Red histogram corresponds to right-lateral faults (total of 30 samples, maximum number of samples per bin: 7), and blue histogram corresponds to left-lateral faults (total of 40 samples, maximum number of samples per bin: 10). Hatched areas denote orientation of faults ruptured by the M6.4 foreshock and M7.1 mainshock of the 2019 sequence (Jin & Fialko, 2020; Fialko & Jin, 2021). Thin magenta line denotes the principal shortening rate axis derived from geodetic data (Fialko & Jin, 2021).

P-axis, consistent with results of inversions for the principal stress and strain rate axes (Yang & Hauksson, 2013; Hauksson & Jones, 2020; Fialko & Jin, 2021).

4 Distribution of dihedral angles

Using information from both the fault strike (constrained by seismicity lineations) and rake (constrained by the composite focal mechanisms) data, one can identify right- and left-lateral faults in the total fault population without any assumptions about the sense of shear stress resolved on the respective faults due to regional tectonic loading. The observed distribution of orientations of active faults in the Ridgecrest area prior to the 2019 earthquake sequence is shown in Figure 4. The two sets of conjugate faults form distinct clusters in a polar histogram (red and blue sectors in Figure 4). Left-lateral faults are well aligned with those ruptured during the July 4 2019 M6.4 foreshock (Fialko & Jin, 2021). Right-lateral faults trend somewhat more northerly compared to the main rupture of the July 5 2019 mainshock, but similar to the initial rupture at the hypocenter of the mainshock suggested by the first motion data (Jin & Fialko, 2020). The axis of the principal shortening rate (Fialko & Jin, 2021) approximately bisects the dihedral angle formed by the conjugate fault planes (Figure 4). The principal compression axis is oriented similar to the principal shortening rate axis (~ 5 degrees east of north) around the hypocentral area of the M7.1 mainshock (Hauksson & Jones, 2020; Fialko & Jin, 2021).

To quantify the range of admissible relative orientations of conjugate faults, I calculate a dihedral angle between every pair of the identified conjugate faults. Figure 5 shows a histogram of dihedral angles 2θ, where θ is an angle between either fault plane and a bisect. Uncertainties in the distribution of dihedral angles of conjugate faults (Figure 5) are estimated using uncertainties in individual fault strikes. Suppose e_i is uncertainty in the slope of a best linear fit for a cluster i, and m is a number of clusters in a given bin j of dihedral angles, $a < 2\theta < b$, where a and b are the minimum and maximum values of samples in a given bin. The standard error of the mean of m
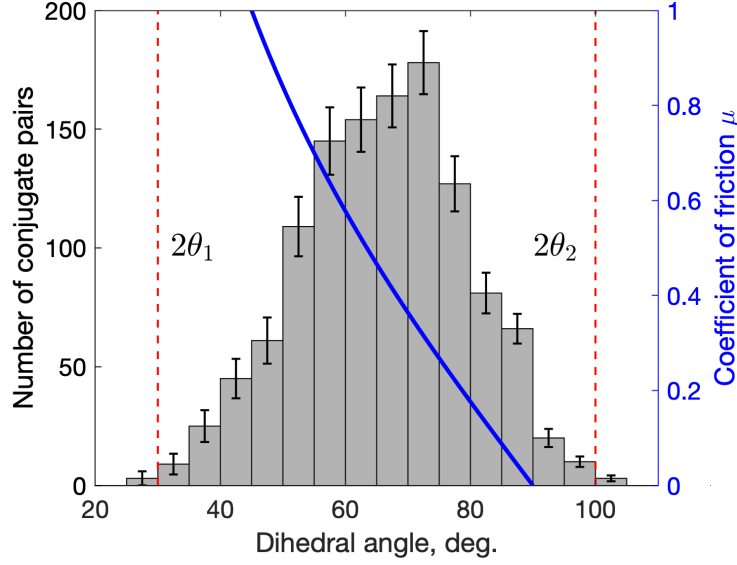
Figure 5. A histogram of dihedral angles between the conjugate strike-slip faults identified in Figure 3. Red vertical lines denote the lower ($2\theta_1$) and upper ($2\theta_2$) bounds on the observed distribution. Blue line (right axis) denotes the coefficient of friction corresponding to conjugate faults that are optimally oriented for failure according to the Mohr-Coulomb criterion, $\mu = 1/\tan(2\theta)$ (Sibson, 1990).

angles is $\epsilon_j = s/\sqrt{m}$, where s is the standard deviation of $e_1, e_2, ..., e_m$ samples (Hogg et al., 2005).

Uncertainties on a number of conjugate pairs for a given bin of dihedral angles are estimated assuming a normal distribution of measured values of $2\theta_j$ with known mean and standard deviation. A probability $p_i(j)$ that a data point θ_i belongs to bin j is:

$$p_i(j) = \int_a^b \frac{1}{\sqrt{2\pi}s_i} \exp\left[-\frac{(\theta_i - z)^2}{2s_i^2}\right] dz. \tag{1}$$

The expected value of data points in a bin is given by a sum of the respective probabilities,

$$E_j = \Sigma_i p_i(j), \tag{2}$$

with the Bernoulli variance given by

$$V_j = \Sigma_i p_i(j)(1 - p_i(j)). \tag{3}$$

The standard deviation is the square root of variance (Hogg et al., 2005),

$$s_j = \sqrt{V_j}. \tag{4}$$

The ratio of the standard deviation to the expected value, $\rho_j = s_j/E_j$, is a proxy for a relative error of the "unobserved count" of samples in each data bin. In Figure 5, uncertainties in the number of dihedral angles per bin are estimated by multiplying the actual bin counts by the respective values of ρ_j calculated using equations 1, 2, 3, and 4.

The distribution of dihedral angles shown in Figure 5 has a peak around 70 degrees, and lower and upper bounds around 30 and 100 degrees, respectively. Assuming a homogeneous background stress, some of the conjugate faults are optimally oriented for failure given the laboratory values of the quasi-static coefficient of friction $\mu \sim 0.6 - 0.8$, while others are not optimally oriented for any reasonable value of μ. It follows that the observed fault orientations require some heterogeneity in the effective fault strength, ambient stress, or both.

5 Role of stress heterogeneity

A locally homogeneous background stress is commonly assumed in inversions for the principal stress orientations (Gephart & Forsyth, 1984; Michael, 1987). There is no physically justified length scale behind this assumption as rock volumes thought to satisfy the assumption of stress homogeneity are chosen based on the density of seismic events (number of events per unit volume) (e.g., Hardebeck & Hauksson, 2001). In the presence of multiple faults and fractures, the assumption of a homogeneous stress is likely violated at small scales ranging from micro-asperities on a fault surface to the macroscopic fault roughness, as predicted by numerical models (Mitchell et al., 2013; Dieterich & Smith, 2009) and observed in deep boreholes intersecting natural faults (e.g., Brudy et al., 1997). Stresses are also known to vary on spatial scales on the order of hundreds of kilometers, as evidenced by regional inversions of the earthquake focal mechanisms (e.g., Yang & Hauksson, 2013), presumably indicating transitions between different tectonic domains. Other factors that may affect stress heterogeneity include e.g. 3-D variations in mechanical properties of the host rocks (Fialko et al., 2002; Barbot et al., 2009).

It is not obvious if the assumption of a constant background stress might be applicable at spatial scales on the order of $10^3 - 10^4$ m (Iio et al., 2017; Alt & Zoback, 2017) that are sampled by faults considered in this study (Figures 3, 2, and S1-S2). To check whether results presented in Figures 4 and 5 could be attributed to stress heterogeneity, I perform several tests. In particular, I examine the distribution of angles between synthetic faults (i.e., faults that have the same sense of slip) as a function of distance between the respective faults. If a relatively broad distribution of dihedral angles (Figure 5) results from spatial variations in the orientation of the principal stress axes, strikes of closely spaced faults should be more similar to each other compared to strikes of more distant faults having the same sense of slip. This would be expected e.g. if faults were optimally oriented with respect to a local stress, but not necessarily to a regional stress. The observed distribution of orientations of synthetic faults as a function of distance between the faults is shown in the Supplementary Figure S3. The data indicate that (i) there is a notable diversity in fault orientations at short (< 10 km) distances, (ii) there is little, if any, systematic increase in the diversity of fault orientations with distance, and (iii) fault orientations exhibit coherence at large (> 30 km) distances.

Previous studies suggested a local rotation of the principal stress axes around the Coso region (northings $N > 40$ km in a local coordinate system used in Figure 3) (Hauksson & Jones, 2020). To investigate the respective possibility, I divided the data into the northern ($N > 40$ km) and southern ($N < 40$ km) sub-sets, and repeated the analysis for each sub-set. Figures S4-S5 show variability in fault strikes vs distance between pairs of synthetic faults, and Figures S6-S7 show the distribution of fault strikes. The northern sub-set shows some correlation between the diversity of fault strikes and distance between synthetic faults, suggesting a possible effect of stress heterogeneity (Figure S4). In part such heterogeneity could be attributed to a long-term fluid pumping at the Coso geothermal plant (Fialko & Simons, 2000; Tymofyeyeva & Fialko, 2015). Also, conjugate faults in the northern sub-set exhibit smaller dihedral angles that are closer to optimal orientations compared to faults in the southern sub-set

(cf. Figures S6 and S7). However, the mean of the left- and right-lateral fault strikes (i.e., the bisect) is not resolvably different between the northern and southern sub-sets, suggesting that a constant regional stress is a viable first-order approximation. The spatial resolution of stress inversions depends on the distribution of seismicity; in areas with enough data (including the epicentral area of the 2019 Ridgecrest earthquakes) the observed variations in the orientation of the principal stress axes are smaller than 10-20 degrees (Fialko & Jin, 2021, see their figure 2), insufficient to explain the observed distribution of dihedral angles (Figure 5) in terms of regional variations in the stress field.

Given that the background tectonic loading is relatively uniform (Floyd et al., 2020; Fialko & Jin, 2021), most of the local stress heterogeneity in the upper crust is likely associated with brittle failure. To quantify effects of stress heterogeneity due to a complex network of randomly oriented faults, I performed numerical simulations in which I varied the fault distribution, the ambient stress, and the effective fault strength.

5.1 Rotation of the principal stress axes due to a complex system of interacting faults

Slip on faults ultimately reduces stress imposed by tectonic loading, but also results in a re-distribution of stress within the brittle crust, with largest stress perturbations typically concentrated around the fault edges (e.g., Martel & Pollard, 1989). To quantify the effects of stress heterogeneity (specifically, the amount of rotation of the principal stress axes) due to a complex fault system, I simulate a network of randomly oriented two-dimensional (plane strain) faults subject to a prescribed remotely applied stress (Figure 6). Each fault is approximated by a linear array of dislocations. The boundary condition on each dislocation is $\tau \leq \mu\sigma'_n$, where τ and σ'_n are respectively the shear and the effective normal stress (normal stress minus the pore fluid pressure) resolved on a dislocation plane, and μ is the local coefficient of friction. Both τ and σ'_n are total stresses that result from the remotely applied stress as well as slip on faults in response to the remotely applied stress. The boundary condition ensures that each fault locally does not violate the Mohr-Coulomb failure criterion. Numerical simulations are performed using a boundary element code TwoDD modified to handle non-linear stress-controlled boundary conditions (Crouch & Starfield, 1983; Fialko & Rubin, 1997). Fault lengths randomly vary in the interval 1-11 km, chosen to approximate the observed distribution of active faults in the Ridgecrest area (Figures 1a and 3). Figure 6 shows an example of a modeled fault distribution. The remotely applied stress has eigenvectors $\sigma_{E,N}$ aligned with the coordinate axes, "east" (E) and "north" (N), such that σ_E=-40 MPa, and σ_N=-160 MPa, similar to the background stress inferred from the observed fault orientations in Ridgecrest (see Discussion section). The maximum compressive stress σ_N is somewhat increased compared to an equilibrium principal stress at which the optimally oriented faults are on the verge of failure, to allow for finite slip on the modeled faults.

Two sets of simulations were performed for each random realization of the fault system, one assuming a constant coefficient of friction ($\mu = 0.6$, Figure 6a,c), and another assuming a variable coefficient of friction ($0.3 < \mu < 0.6$, Figure 6b,d). The assumed range of the coefficient of friction spans the transition from strong to weak faults (e.g., Lockner et al., 2011; Collettini et al., 2009). The top panels in Figure 6 show the slip magnitude and the bottom panels show the orientation of the principal compression axis (tick marks) and its rotation due to slip on faults (color). The modeled faults essentially approximate shear cracks with a constant stress drop. In case of spatially constant friction, only the faults that happened to be nearly optimally oriented for failure become activated by the applied remote stress field, as expected (Figure 6a). In case of variable friction, a more diverse population of faults is brought
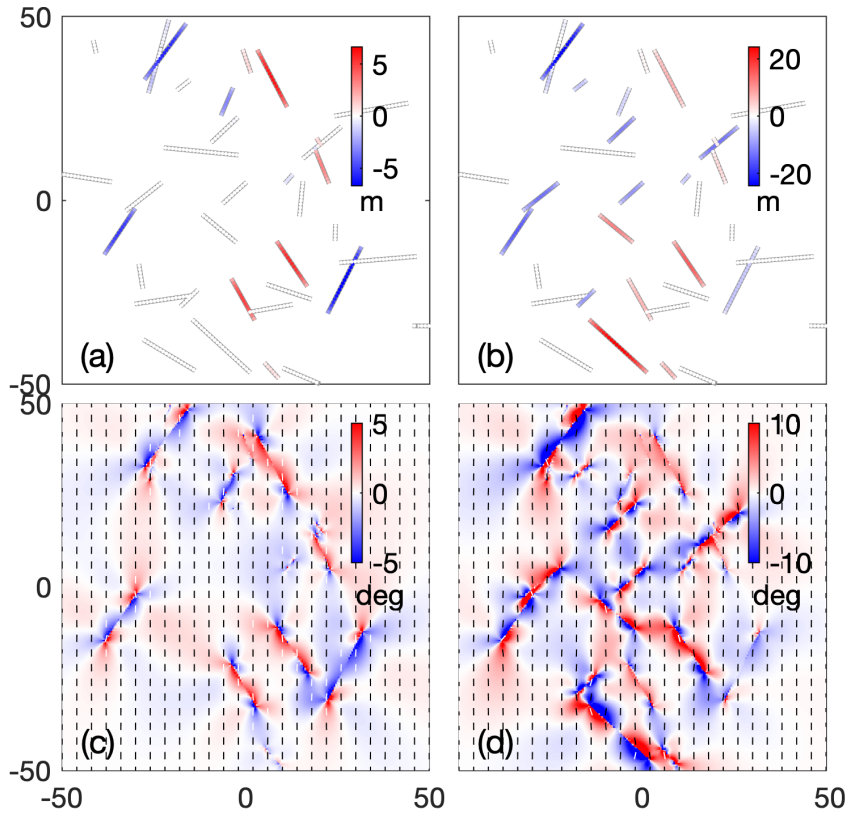
Figure 6. Numerical simulations of a system of randomly oriented faults activated by the applied remote stress field. (a,c) Geometry of the fault network. Color denotes the slip magnitude. Right-lateral slip is positive and left-lateral slip is negative. (b,d) Orientation of the maximum compression axis (tickmarks) and rotation caused by fault slip (color). Counterclockwise rotation is deemed positive. (a,c) Constant coefficient of friction, $\mu = 0.6$. (b,d) Variable coefficient of friction, $0.3 < \mu < 0.6$. Calculations assume the Young's modulus of 50 GPa, and the Poisson ratio of 0.25. Coordinate axes are in km.

to failure (Figure 6b). For the same remote stress, reductions in μ give rise to larger static stress drops and slip magnitudes on pre-existing faults. Faults with a constant stress drop produce a weak stress singularity at the fault tips (e.g., Pollard & Segall, 1987; Fialko, 2015). Despite such a singularity, only limited rotation of the principal stress axis is observed in the surrounding medium. In case of constant friction, the stress rotation is essentially negligible (Figure 6c). In case of heterogeneous friction, the stress rotation on average does not exceed ~ 10 degrees, and is limited to relatively small areas around the fault tips (Figure 6d). Increases in the magnitude of the remotely applied shear and mean stresses result in stress rotations that are smaller still, as the ratio of stress perturbations due to fault slip to the absolute background stress decreases.

Results presented above suggest that the observed distribution of orientations of active faults in the Ridgecrest area (Figures 1a, 3, and 5) is unlikely explained in terms of spatial heterogeneity of stresses acting in the seismogenic zone.

6 Role of strength heterogeneity

It may be argued that small earthquakes that comprise quasi-linear clusters (Figures 1a, 2, 3, and S1-S2) are primarily governed by the rate and state friction (Dieterich, 2015) and are not subject to strong dynamic weakening, so that the peak yield stress is comparable to the background stress (Fialko, 2015). In this case, one can interpret the observed range of fault orientations (Figure 5) in terms of activation ($\theta > \theta_1$) and de-activation ($\theta > \theta_2$) of pre-existing or newly created faults. It is generally recognized that the continental Earth's crust is pervasively faulted and contains cracks, fractures and other structural defects that can serve as potential slip surfaces over a broad range of sizes and orientations (Sykes, 1978; Sibson, 1990).

6.1 Slip on immature sub-optimally oriented faults: Theory

Given a stress field with axes of the effective principal stresses σ_1' and σ_3' parallel to the Earth's surface, a condition for activation of pre-existing strike-slip faults is (Sibson, 1985, 1990):

$$R = \frac{\sigma_1'}{\sigma_3'} = \frac{1 + \mu \cot \theta}{1 - \mu \tan \theta}, \tag{5}$$

where R is the effective stress ratio, σ_1' is the effective maximum compressive stress (maximum compressive stress minus the pore pressure P), σ_3' is the effective minimum compressive stress, μ is the coefficient of friction, and θ is the angle between a fault plane and the maximum compression axis. Equation 5 assumes the Mohr-Coulomb failure criterion, vertical orientation of the intermediate principal stress, and negligible (compared to friction) cohesion on a potential slip plane.

Equation 5 is typically under-determined as the number of unknowns (e.g., σ_1', σ_3' and μ) is greater than the number of observables (such as angles between conjugate faults or between faults and the principal stress axes). In case of the Ridgecrest seismicity, several unique conditions may allow one to resolve this uncertainty. First, a transtensional stress regime manifested by a mix of strike-slip and normal focal mechanisms (Hauksson & Jones, 2020), including spatially overlapping strike-slip and normal earthquake ruptures (Jin & Fialko, 2020) indicates that the maximum compressive (σ_1') and intermediate (σ_2') principal stresses are essentially of the same magnitude. Under the usual assumption that one of the principal stresses is vertical, the transtensional stress regime implies that both σ_1' and σ_2' should approximately equal the effective lithostatic stress, $\rho_c g z - P$, where ρ_c is the average density of the upper crust, g is the gravitational acceleration, and z is depth. Second, assuming that the lower and upper bounds of the observed distribution of dihedral angles (Figure 5) correspond to

activation (θ_1) and de-activation (θ_2) of pre-existing faults, one can estimate a possible range of variations in the coefficient of friction on activated faults, $\mu_1 < \mu < \mu_0$. The lower bound on μ is given by

$$\mu_1 = \frac{1}{\tan(\theta_1 + \theta_2)}. \tag{6}$$

The minimum failure envelope $\tau = \mu_1 \sigma'_n$, where σ'_n and τ are respectively the effective normal and shear stresses resolved on a fault, intersects the Mohr circle (Twiss & Moores, 1992, p. 141) at points corresponding to fault orientations $2\theta_1$ and $2\theta_2$. A fault orientation that maximizes an excursion beyond the minimum failure envelope is given by an average of the activation and de-activation angles θ_1 and θ_2. Substituting equation 6 into equation 5, and taking θ to be equal to either θ_1 or θ_2, one obtains expressions for the critical stress ratio R^* and the effective minimum compressive stress σ'_3:

$$R^* = \frac{1 + \mu_1 \cot \theta_1}{1 - \mu_1 \tan \theta_1} = \frac{1 + \mu_1 \cot \theta_2}{1 - \mu_1 \tan \theta_2}, \tag{7}$$

$$\sigma'_3 = \sigma'_1 / R^*. \tag{8}$$

The coefficient of friction μ_1 provides a lower bound on the frictional strength of activated sub-optimally oriented faults. Faults that are oriented at more acute angles with respect to the principal compression axis can be on the verge of failure if they have a higher coefficient of friction, with an upper bound μ_0 that corresponds to an optimal fault orientation. The upper bound on μ can be found from the following relationship between the stress ratio R and the coefficient of friction that corresponds to an optimal orientation (Sibson, 1985):

$$R = \left(\sqrt{1 + \mu_0^2} + \mu_0 \right)^2. \tag{9}$$

Solving for real non-negative values of μ_0 gives rise to

$$\mu_0 = \frac{R^* - 1}{2\sqrt{R^*}}. \tag{10}$$

Figure 7 shows a Mohr circle diagram for the state of stress that satisfies the above constraints as well as the assumption of a hydrostatic pore pressure (Townend & Zoback, 2000) ($P = \rho_w g z$, where ρ_w is the density of water), at a reference depth of 7 km. The latter is within the estimated range of the hypocentral depth of the M7.1 Ridgecrest earthquake (3-8 km) (Hauksson & Jones, 2020). It also approximately corresponds to the middle of the seismogenic layer, so that the absolute stresses shown in Figure 7 represent stresses averaged over the thickness of the seismogenic layer. As one can see from Figure 7, the estimated stress ratio is $R^* \approx 3$, the depth-averaged shear stresses resolved on seismically active faults are 25-40 MPa, and the inferred range of in situ coefficient of friction is $0.4 < \mu < 0.6$.

7 Discussion

High-end values of the estimated coefficient of friction are in agreement with laboratory measurements of quasi-static friction of most rock types (Byerlee, 1978), and may correspond to the formation of new faults or activation of pre-existing suitably oriented faults in the ECSZ (Figure 7). The value of $\mu \sim 0.6$ is also consistent with models suggesting that faults ruptured in the 2019 sequence were initiated at or near to an optimal orientation of $\sim 30°$ with respect to the principal compression axis at the inception of the ECSZ, and subsequently rotated to their current (sub-optimal)
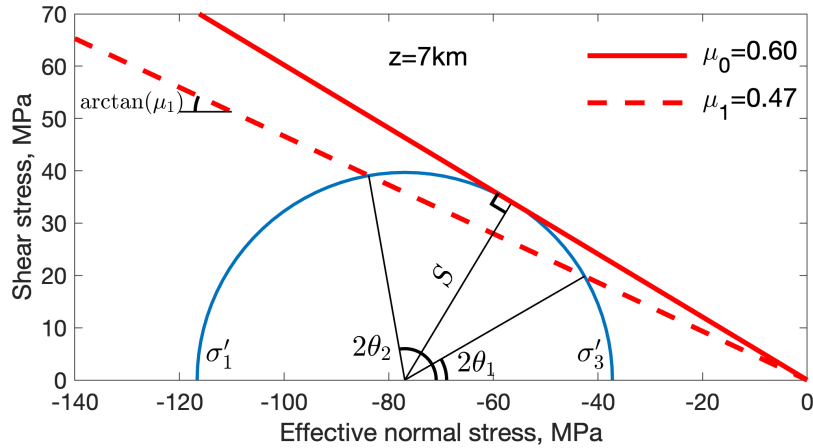
Figure 7. The estimated state of stress in the hypocentral region of the 2019 Ridgecrest earthquakes. Blue curve (the Mohr circle) denotes variations in shear stress on potential slip planes as a function of a dihedral angle 2θ between conjugate slip planes (or angle θ between a slip plane and the maximum compression axis). Radius of the Mohr circle represents the maximum shear stress, $S = |\sigma_1' - \sigma_3'|/2$. Red lines are the Mohr-Coulomb failure envelopes corresponding to activation of pre-existing faults (μ_1, dashed line), and generation of new faults (μ_0, solid line). Calculations assume $\rho_c = 2.7 \times 10^3$ kg/m^3, $\rho_w = 10^3$ kg/m^3, and $g = 9.8$ m/s^2.

orientations (Fialko & Jin, 2021). The model of Fialko and Jin (2021) implies that the newly formed or activated faults progressively weakened as they continued to accumulate slip and rotate away from their optimal orientation due to the long-term tectonic motion. Hauksson and Jones (2020) proposed that the orientation of the 2019 earthquake ruptures with respect to the present-day principal compression axis might be explained assuming higher values of the stress ratio ($R > 5$) and the coefficient of friction ($\mu = 0.75$). Such high values however appear to be inconsistent with the observed transtensional stress regime in the Ridgecrest-Coso area, and would require pore fluid pressures close to the least compressive stress. Also, a high coefficient of friction would imply a peak in dihedral angles of the regional fault population around the respective optimal value (~ 55 degrees for $\mu = 0.75$) which is not observed (Figure 5). Note that orientations of the 2019 ruptures (Figures 1b and 4) are within the documented range of a regional data set (Figure 5), so that results presented in this study apply to the observed geometry of the 2019 earthquakes.

The inferred value of μ_0 (Figure 7) is also in agreement with observations of injection-induced seismicity in the central US that reveal ubiquitous dihedral angles of $\sim 60°$ (Schoenball & Ellsworth, 2017; Alt & Zoback, 2017; Skoumal et al., 2019). Such observations are consistent with the idea that stable continental interiors can support stresses on the order of hundreds of megapascals predicted by the strong fault theory. A relatively broad distribution of dihedral angles in the Ridgecrest area with a peak around $\sim 70 - 75°$ (Figure 5) is however markedly different from a highly clustered distribution observed in the central US (Schoenball & Ellsworth, 2017; Skoumal et al., 2019), suggesting differences in the stress regime and the effective strength of the bulk of the seismogenic crust. In part such differences could be attributed to different tectonic settings and loading conditions. Specifically, seismicity in the central US exemplifies a stable continental interior responding to the anthropogenically induced increases in pore fluid pressure (e.g., Weingarten et al., 2015). In contrast, seismicity in

the Ridgecrest area (Figure 1) is associated with a nascent plate boundary responding to increases in tectonic strain (Nur et al., 1993; Tymofyeyeva & Fialko, 2015; Floyd et al., 2020; Fialko & Jin, 2021). The "developing plate boundary" environment is arguably more relevant for investigating the evolution of fault strength as a function of fault maturity, and may provide useful insights into a poorly understood transition from "strong" to "weak" faults.

The low-end values of the estimated range of the coefficient of friction (μ_1, see equation 6 and Figures 5 and 7) provide some quantitative measure of the degree of weakening associated with fault evolution as a function of tectonic strain. The average shear strain ε accommodated by the ECSZ since its inception 6-10 Ma is on the order of 10-20% (Fialko & Jin, 2021). In a continuum representation of brittle failure such as "seismic flow" of rocks (Riznichenko, 1965), one can define an average rate of tectonic strain softening, $\partial\mu/\partial\varepsilon$. Taking $\partial\mu \approx \mu_0 - \mu_1$, $\partial\mu/\partial\varepsilon$ is estimated to be on the order of unity. A moderate reduction in the coefficient of friction suggested by the analysis of fault orientations (Figures 4, 5 and 7) may be indicative of an onset of various weakening mechanisms with an increasing cumulative fault slip, such as mineral alteration, ultra-comminution, pressurization of fault zone fluids, etc. (e.g., Imber et al., 1997; Reches & Lockner, 2010; Lacroix et al., 2015). Largest faults in the system might also experience dynamic weakening (Jin & Fialko, 2020).

Note that some variability in the coefficient of friction that could contribute to the observed diversity of fault orientations (Figures 3 and 5) is naturally expected due to dependence of friction on composition, normal stress, temperature, and other environmental variables (Stesky et al., 1974; Byerlee, 1978; Mitchell et al., 2013, 2015, 2016; Collettini et al., 2019). A key distinction with the "cumulative slip-weakening" model is that the latter predicts a systematic dependence of the effective fault strength on fault maturity. In particular, faults in the ECSZ that are currently less optimally oriented for slip were likely activated before faults that are currently well oriented with respect to the present-day stress field. While it may be difficult to determine the fault age or a cumulative offset, especially for small faults that are only expressed in micro-seismicity and don't yet have a surface expression (Figure 1a), I note that faults that produced the 2019 sequence are on the "long/less well-oriented" end of the distribution of active faults in the study area (Figures 1b and 5), consistent with a notion that for developing faults, the fault length correlates with the fault age (e.g., Cowie & Scholz, 1992).

Fault orientations could also be affected by local or regional anisotropy in the mechanical properties of the upper crust. The effects of anisotropy on the distribution of dihedral angles between conjugate faults depend on the relative orientations of the anisotropic fabric and the principal compressive stress. In particular, increased dihedral angles may be produced when σ_1' is oblique to anisotropy (e.g., Peacock & Sanderson, 1992). This mechanism would imply a strong sub-vertical foliation or layering throughout the seismogenic layer, which is not observed. Other factors such as an agreement between the orientation of the σ_1' axis and a bisect to the dihedral angles, and approximately equal numbers of dextral and sinistral faults (Figure 4), as well as the diversity of fault orientations, including both strike-slip and dip-slip faults, suggest that anisotropy does not exert a first-order control on fault orientations in the study area.

Estimates of shear stress based on the Mohr-Coulomb theory are upper bounds in that they define the maximum shear stress the upper crust can support before new faults are formed. In the presence of mature well-slipped faults, the average shear stress resolved on the respective faults can be well below the static Mohr-Coulomb failure envelope due to the effects of dynamic rupture (e.g., Noda et al., 2009; Thomas et al., 2014; Fialko, 2015). The long-term reduction in strength depends on the magnitude of stress concentration ahead of the rupture front, and dynamic weakening behind the

rupture front during individual seismic events (Kirkpatrick & Shipton, 2009; Di Toro et al., 2011; Rubino et al., 2017). Both factors are expected to scale with the rupture size. Over geologic time, mature faults localize tectonic strain and may not be oriented with respect to the principal stress axes in any predictable fashion, other that the sense of shear stress resolved on a fault should be the same as the sense of fault slip.

The method proposed in this study relies on relative orientations of small developing immature faults distributed throughout the seismogenic layer, so that the effects of stress concentration and dynamic weakening, if any, should be minimal. It should be mentioned that dihedral angles between conjugate faults are uniquely related to the coefficient of friction only in case of newly formed faults; a re-activation of pre-existing faults depends on other factors that affect the effective fault strength, such as e.g. the pore fluid pressure. The lower bound on the coefficient of friction μ_1 (Figures 5 and 7) should therefore be considered an effective residual friction that accounts for all relevant weakening mechanisms. A distribution of dihedral angles can be evaluated for strike-slip as well as dip-slip fault systems. Estimation of the magnitude of shear stress further requires special conditions such as a 2-D state of stress (equal magnitudes of two of the principal stress components corresponding to e.g. transtensional or transpressional stress regimes).

The above conditions appear to be met in the area around Ridgecrest (Figures 1 and 3), allowing a unique estimate of the magnitude of absolute stresses in the seismogenic crust. The depth-averaged shear stress S is on the order of a few tens of megapascals (see Figure 7). This is well below the values of shear stress measured in deep boreholes and suggested by seismic observations in the stable continental crust (e.g., Brudy et al., 1997; Townend & Zoback, 2000; Schoenball & Ellsworth, 2017), but similar to values suggested for the San Andreas Fault (SAF) based on the borehole measurements (Lockner et al., 2011) and independent constraints such as the heat flow data (Lachenbruch & Sass, 1980) and stress perturbations due to topography (Fialko et al., 2005). Despite similar values of the driving shear stress, active faults in the Ridgecrest area may be considered to be relatively strong compared to the SAF because of the transtensional stress regime in the ECSZ versus transpressional regime on the SAF. The magnitude of shear stress in the study area thus falls in between predictions of the strong and weak fault theories.

8 Conclusions

Precisely determined relative locations of small and intermediate size earthquakes often reveal lineated structures likely illuminating active faults at depth. Quasi-linear clusters of earthquakes can be used to constrain fault orientations (e.g., strike and dip angles), which, in combination with information provided by the composite focal mechanisms, may allow one to quantify relative orientations of active conjugate faults. Dihedral angles formed by the conjugate fault planes carry information about the heterogeneity in the ambient stress field and the fault strength, as well as the orientation and (under certain conditions) the magnitude of the principal stresses. I demonstrate the proposed method using data from the Eastern California Shear Zone near the town of Ridgecrest that hosted a series of strong earthquakes in July of 2019. The data analysis indicates that the attitudes of small- to medium-sized faults (that sample in situ stresses on spatial wavelengths on the order of kilometers) are essentially the same as those of the M6-M7 earthquakes of the 2019 Ridgecrest sequence that ruptured the entire seismogenic layer (thereby sampling stresses on spatial wavelengths on the order of tens of kilometers). I use statistics of dihedral angles between active faults expressed in the background (prior to July 2019) seismicity to estimate the effective fault strength and the absolute shear stress acting at seismogenic depths. The inferred range of the coefficient of friction is $0.4 < \mu < 0.6$, and the depth-average shear stress is 25-40 MPa. A possible interpretation of the observed distribution of

dihedral angles is that the new faults are formed (or existing faults are activated) at optimal angles with respect to the maximum compression axis, and are progressively weakened as they continue to accumulate slip and rotate away from the optimal orientation due to a long-term tectonic motion. Results presented in this study suggest that a transition from "strong" to "weak" faults may initiate at the early stages of formation of a plate boundary, and involve relatively low total offsets. The proposed method can be used to assess the magnitude of shear stress acting at seismogenic depths in other actively deforming areas expressed in abundant microseismicity, but lacking well-developed mature faults. Quasi-linear clusters of earthquakes and their composite focal mechanisms can also be used to improve robustness of inversions for the orientation of the principal stress axes.

Data Availability Statement

The data that support the findings of this study are openly available in the Southern California Earthquake Data Center (SCEDC) repository (doi: 10.7909/C3WD3xH1) at `https://scedc.caltech.edu/data/alt-2011-yang-hauksson-shearer.html` and `https://scedc.caltech.edu/data/alt-2011-dd-hauksson-yang-shearer.html`. Data are available through Yang et al. (2012) and Hauksson et al. (2012). The SCEDC and SCSN are funded through U.S. Geological Survey Grant G20AP00037, and the Southern California Earthquake Center, which is funded by NSF Cooperative Agreement EAR-0529922 and USGS Cooperative Agreement 07HQAG0008.

References

Allmann, B. P., & Shearer, P. M. (2009). Global variations of stress drop for moderate to large earthquakes. *J. Geophys. Res.*, *114*, B01310.

Alt, R. C., & Zoback, M. D. (2017). In situ stress and active faulting in Oklahoma. *Bull. Seism. Soc. Am.*, *107*(1), 216–228.

Anderson, E. M. (n.d.). *The dynamics of faulting and dike formation with application to Britain, year = 1951.* Edinburgh: 206 pp., Oliver and Boyd.

Angelier, J. (1994). Fault slip analysis and palaeostress reconstruction. In *Continental deformation* (pp. 53–100).

Ankerst, M., Breunig, M. M., Kriegel, H.-P., & Sander, J. (1999). OPTICS: ordering points to identify the clustering structure. *ACM Sigmod record*, *28*(2), 49–60.

Araújo, A. M., & Oliveira, M. M. (2020). A robust statistics approach for plane detection in unorganized point clouds. *Pattern Recognition*, *100*, 107–115.

Barbot, S., Fialko, Y., & Sandwell, D. (2009). Three-dimensional models of elasto-static deformation in heterogeneous media, with applications to the Eastern California Shear Zone. *Geophys. J. Int.*, *179*, 500–520.

Barton, N. (1976). The shear strength of rock and rock joints. *International Journal of rock mechanics and mining sciences & Geomechanics abstracts*, *13*, 255–279.

Brown, K. M., & Fialko, Y. (2012). "Melt welt" mechanism of extreme weakening of gabbro at seismic slip rates. *Nature*, *488*, 638–641.

Brudy, M., Zoback, M., Fuchs, K., Rummel, F., & Baumgartner, J. (1997). Estimation of the complete stress tensor to 8 km depth in the KTB scientific drill holes: Implications for crustal strength. *J. Geophys. Res.*, *102*, 18435–18475.

Byerlee, J. (1978). Friction of rock. *Pure Appl. Geophys.*, *116*, 615–626.

Chester, J. S., Chester, F. M., & Kronenberg, A. K. (2005). Fracture surface energy of the Punchbowl fault, San Andreas system. *Nature*, *437*, 133–136.

Choy, G. L., & Boatwright, J. L. (1995). Global patterns of radiated seismic energy and apparent stress. *J. Geophys. Res.*, *100*, 18205–18228.

Collettini, C., Niemeijer, A., Viti, C., & Marone, C. (2009). Fault zone fabric and fault weakness. *Nature*, *462*, 907–910.

Collettini, C., & Sibson, R. H. (2001). Normal faults, normal friction? *Geology*, *29*, 927–930.

Collettini, C., Tesei, T., Scuderi, M. M., Carpenter, B. M., & Viti, C. (2019). Beyond Byerlee friction, weak faults and implications for slip behavior. *Earth Planet. Sci. Lett.*, *519*, 245–263.

Cowie, P. A., & Scholz, C. H. (1992). Growth of faults by accumulation of seismic slip. *J. Geophys. Res.*, *97*, 11,085–11,095.

Crouch, S. L., & Starfield, A. M. (1983). *Boundary element methods in solid mechanics*. Boston: George Allen and Unwin.

Dieterich, J. (2015). Applications of Rate- and State-Dependent Friction to Models of Fault Slip and Earthquake Occurrence. In G. Schubert (Ed.), *Treatise on geophysics, 2nd. ed., vol. 4* (pp. 93–110). Elsevier Ltd., Oxford.

Dieterich, J. H. (1981). Mechanical behavior of crustal rocks. In N. L. Carter, M. Friedman, J. M. Logan, & D. W. Stearns (Eds.), *Mechanical behavior of crustal rocks: the handin volume* (Vol. 24, pp. 103–120). Washington, DC: American Geophysical Union.

Dieterich, J. H., & Smith, D. E. (2009). Nonplanar faults: Mechanics of slip and off-fault damage. In *Mechanics, structure and evolution of fault zones* (pp. 1799–1815). Springer.

Di Toro, G., Han, R., Hirose, T., De Paola, N., Nielsen, S., Mizoguchi, K., ... Shimamoto, T. (2011). Fault lubrication during earthquakes. *Nature*, *471*(7339), 494–498.

Dokka, R. K., & Travis, C. J. (1990). Role of the Eastern California shear zone in accommodating Pacific-North American plate motion. *Geophys. Res. Lett.*, *17*, 1323–1327.

Duputel, Z., Rivera, L., Fukahata, Y., & Kanamori, H. (2012). Uncertainty estimations for seismic source inversions. *Geophys. J. Int.*, *190*, 1243–1256.

DuRoss, C. B., Gold, R. D., Dawson, T. E., Scharer, K. M., Kendrick, K. J., Akciz, S. O., ... others (2020). Surface displacement distributions for the July 2019 Ridgecrest, California, earthquake ruptures. *Bull. Seism. Soc. Am.*, *110*, 1400–1418.

Fialko, Y. (2004). Evidence of fluid-filled upper crust from observations of post-seismic deformation due to the 1992 M_w7.3 Landers earthquake. *J. Geophys. Res.*, *109*, B08401, 10.1029/2004JB002985.

Fialko, Y. (2015). Fracture and Frictional Mechanics - Theory. In G. Schubert (Ed.), *Treatise on geophysics, 2nd. ed., vol. 4* (pp. 73–91). Elsevier Ltd., Oxford.

Fialko, Y., & Jin, Z. (2021). Simple shear origin of the cross-faults ruptured in the 2019 Ridgecrest earthquake sequence. *Nature Geoscience*. doi: doi.org/10.1038/s41561-021-00758-5

Fialko, Y., & Khazan, Y. (2005). Fusion by earthquake fault friction: Stick or slip? *J. Geophys. Res.*, *110*, B12407, doi:10.1029/2005JB003869.

Fialko, Y., Rivera, L., & Kanamori, H. (2005). Estimate of differential stress in the upper crust from variations in topography and strike along the San Andreas fault. *Geophys. J. Int.*, *160*, 527–532.

Fialko, Y., Sandwell, D., Agnew, D., Simons, M., Shearer, P., & Minster, B. (2002). Deformation on nearby faults induced by the 1999 Hector Mine earthquake. *Science*, *297*, 1858–1862.

Fialko, Y., & Simons, M. (2000). Deformation and seismicity in the Coso geothermal

area, Inyo County, California: Observations and modeling using satellite radar interferometry. *J. Geophys. Res.*, *105*, 21781–21793.

Fialko, Y. A., & Rubin, A. M. (1997). Numerical simulation of high pressure rock tensile fracture experiments: Evidence of an increase in fracture energy with pressure? *J. Geophys. Res.*, *102*, 5231–5242.

Floyd, M., Funning, G., Fialko, Y. A., Terry, R. L., & Herring, T. (2020). Survey and Continuous GNSS in the vicinity of the July 2019 Ridgecrest earthquakes. *Seismol. Res. Lett.*, *91*, 2047–2054.

Gephart, J. W., & Forsyth, D. W. (1984). An improved method for determining the regional stress tensor using earthquake focal mechanism data: Application to the San Fernando earthquake sequence. *J. Geophys. Res.*, *89*, 9305–9320.

Goldsby, D., & Tullis, T. (2011). Flash heating leads to low frictional strength of crustal rocks at earthquake slip rates. *Science*, *334*, 216-218.

Han, R., Shimamoto, T., Hirose, T., Ree, J.-H., & Ando, J. (2007). Ultralow friction of carbonate faults caused by thermal decomposition. *Science*, *316*, 878–881.

Hardebeck, J. L., & Hauksson, E. (2001). Crustal stress field in southern California and its implications for fault mechanics. *J. Geophys. Res.*, *106*, 21859–21882.

Hardebeck, J. L., & Shearer, P. M. (2002). A new method for determining first-motion focal mechanisms. *Bull. Seism. Soc. Am.*, *92*, 2264–2276.

Hauksson, E., & Jones, L. (2020). Seismicity, stress state, and style of faulting of the Ridgecrest-Coso region from the 1930s through 2019: Seismotectonics of an evolving plate boundary segment. *Bull. Seism. Soc. Am.*, *110*, 1457–1473. doi: 10.1785/0120200051

Hauksson, E., Jones, L., & Hutton, K. (2002). The 1999 M_w 7.1 Hector Mine, California, earthquake sequence: Complex conjugate strike-slip faulting. *Bull. Seism. Soc. Am.*, *92*, 1154–1170.

Hauksson, E., Yang, W., & Shearer, P. M. (2012). Waveform relocated earthquake catalog for Southern California (1981 to 2011). *Bull. Seism. Soc. Am.*, *102*(5), 2239–2244. doi: 10.1785/0120120010

Hogg, R. V., McKean, J., & Craig, A. T. (2005). *Introduction to mathematical statistics, 6th edition.* Pearson Education.

Iio, Y., Yoneda, I., Sawada, M., Miura, T., Katao, H., Takada, Y., ... Horiuchi, S. (2017). Which is heterogeneous, stress or strength? An estimation from high-density seismic observations. *Earth, Planets and Space*, *69*(1), 1–16.

Imber, J., Holdsworth, R., Butler, C., & Lloyd, G. (1997). Fault-zone weakening processes along the reactivated Outer Hebrides Fault Zone, Scotland. *Journal of the Geological Society*, *154*, 105–109.

Jennings, C., & Bryant, W. (2010). Fault activity map of california. *California Division of Mines and Geology*. (Geologic Data Map No. 6)

Jin, Z., & Fialko, Y. (2020). Finite slip models of the 2019 Ridgecrest earthquake sequence constrained by space geodetic data and aftershock locations. *Bull. Seism. Soc. Am.*, *110*, 1660–1679. doi: 10.1785/0120200060

Kirkpatrick, J., & Shipton, Z. (2009). Geologic evidence for multiple slip weakening mechanisms during seismic slip in crystalline rock. *J. Geophys. Res.*, *114*, B12401.

Lachenbruch, A. H., & Sass, J. H. (1980). Heat flow and energetics of the San Andreas fault zone. *J. Geophys. Res.*, *85*, 6185–6222.

Lacroix, B., Tesei, T., Oliot, E., Lahfid, A., & Collettini, C. (2015). Early weakening processes inside thrust fault. *Tectonics*, *34*, 1396–1411.

Lockner, D. A., Byerlee, J., Kuksenko, V., Ponomarev, A., & Sidorin, A. (1992). Observations of quasistatic fault growth from acoustic emissions. In B. Evans & T. Wong (Eds.), *Fault mechanics and transport properties of rocks* (pp. 3–31). Academic, San Diego, CA, USA.

Lockner, D. A., Morrow, C., Moore, D., & Hickman, S. (2011). Low strength of deep San Andreas fault gouge from SAFOD core. *Nature*, *472*(7341), 82–85.

Marone, C. (1998). Laboratory-derived friction laws and their application to seismic faulting. *Annu. Rev. Earth Planet. Sci.*, *26*, 643–696.

Martel, S. J., & Pollard, D. D. (1989). Mechanics of slip and fracture along small faults and simple strike-slip fault zones in granitic rock. *J. Geophys. Res.*, *94*, 9417–9428.

McClusky, S., Bjornstad, S., Hager, B., King, R., Meade, B., Miller, M., . . . Souter, B. (2001). Present day kinematics of the Eastern California Shear Zone from a geodetically constrained block model. *Geophys. Res. Lett.*, *28*, 3369–3372.

Michael, A. J. (1987). Use of focal mechanisms to determine stress: a control study. *J. Geophys. Res.*, *92*, 357–368.

Mitchell, E., Fialko, Y., & Brown, K. (2015). Frictional properties of gabbro at conditions corresponding to slow slip events in subduction zones. *Geochemistry, Geophysics, Geosystems*, *16*(11), 4006–4020.

Mitchell, E., Fialko, Y., & Brown, K. M. (2013). Temperature dependence of frictional healing of Westerly granite: experimental observations and numerical simulations. *Geochemistry, Geophysics, Geosystems*, *14*, 567–582.

Mitchell, E., Fialko, Y., & Brown, K. M. (2016). Velocity-weakening behavior of Westerly granite at temperature up to 600° C. *J. Geophys. Res.*, *121*, 6932–6946.

Mount, V., & Suppe, J. (1987). State of stress near the San Andreas fault: Implications for wrench tectonics. *Geology*, *15*, 1143–1146.

Noda, H., Dunham, E., & Rice, J. R. (2009). Earthquake ruptures with thermal weakening and the operation of major faults at low overall stress levels. *J. Geophys. Res.*, *114*, B07302.

Nur, A., Ron, H., & Beroza, G. (1993). The nature of the Landers-Mojave earthquake line. *Science*, *261*, 201–203.

Nur, A., Ron, H., & Scotti, O. (1986). Fault mechanics and the kinematics of block rotations. *Geology*, *14*, 746–749.

Peacock, D., & Sanderson, D. (1992). Effects of layering and anisotropy on fault geometry. *Journal of the Geological Society*, *149*, 793–802.

Plumb, R. A., & Hickman, S. H. (1985). Stress-induced borehole elongation: A comparison between the four-arm dipmeter and the borehole televiewer in the Auburn geothermal well. *J. Geophys. Res.*, *90*, 5513–5521.

Pollard, D. D., & Segall, P. (1987). Theoretical displacements and stresses near fractures in rock: With applications to faults, joints, veins, dikes, and solution surfaces. In B. K. Atkinson (Ed.), *Fracture mechanics of rock* (pp. 277–350). London: Academic Press.

Reches, Z., & Lockner, D. A. (2010). Fault weakening and earthquake instability by powder lubrication. *Nature*, *467*(452-U102 DOI: 10.1038/nature09348).

Rice, J. R. (1992). Fault stress states, pore pressure distribution, and the weakness of the San Andreas Fault. In B. Evans & T. Wong (Eds.), *Fault mechanics and transport properties of rocks* (pp. 475–503). Academic, San Diego, CA, USA.

Rice, J. R. (2006). Heating and weakening of faults during earthquake slip. *J. Geophys. Res.*, *111*, B05311.

Riznichenko, Y. V. (1965). The flow of rocks as related to seismicity. *Dokl. Akad. Nauk SSSR*, *161*(1), 96–98.

Ross, Z. E., Idini, B., Jia, Z., Stephenson, O. L., Zhong, M., Wang, X., . . . others (2019). Hierarchical interlocked orthogonal faulting in the 2019 Ridgecrest earthquake sequence. *Science*, *366*(6463), 346–351.

Rubino, V., Rosakis, A., & Lapusta, N. (2017). Understanding dynamic friction through spontaneously evolving laboratory earthquakes. *Nature communications*, *8*(1), 1–13.

Schnabel, R., Wahl, R., & Klein, R. (2007). Efficient RANSAC for point-cloud shape detection. In *Computer graphics forum* (Vol. 26, pp. 214–226).

Schoenball, M., & Ellsworth, W. L. (2017). A systematic assessment of the spa-

tiotemporal evolution of fault activation through induced seismicity in Oklahoma and southern Kansas. *J. Geophys. Res.*, *122*(12), 10–189.

Scholz, C. H. (2000). Evidence for a strong San Andreas fault. *Geology*, *28*(2), 163–166.

Scholz, C. H. (2019). *The mechanics of earthquakes and faulting.* New York, NY: 3rd Ed., 493 pp., Cambidge Univ. Press.

Sibson, R. H. (1985). A note on fault reactivation. *J. Struct. Geol.*, *7*(6), 751–754.

Sibson, R. H. (1990). Rupture nucleation on unfavorably oriented faults. *Bull. Seism. Soc. Am.*, *80*, 1580–1604.

Sibson, R. H. (2004). Controls on maximum fluid overpressure defining conditions for mesozonal mineralisation. *J. Struct. Geol.*, *26*(6-7), 1127–1136.

Sieh, K., Jones, L., Hauksson, E., Hudnut, K., Eberhart-Phillips, D., Heaton, T., . . . others (1993). Near-field investigations of the Landers earthquake sequence. *Science*, *260*, 171–176.

Skoumal, R. J., Kaven, J. O., & Walter, J. I. (2019). Characterizing seismogenic fault structures in Oklahoma using a relocated template-matched catalog. *Seismol. Res. Lett.*, *90*(4), 1535–1543.

Sobolev, S. V., & Babeyko, A. Y. (2005). What drives orogeny in the Andes? *Geology*, *33*(8), 617–620.

Stern, R. J., & Gerya, T. (2018). Subduction initiation in nature and models: A review. *Tectonophysics*, *746*, 173–198.

Stesky, R., Brace, W., Riley, D., & Robin, P.-Y. (1974). Friction in faulted rock at high temperature and pressure. *Tectonophysics*, *23*, 177–203.

Sykes, L. R. (1978). Intraplate seismicity, reactivation of preexisting zones of weakness, alkaline magmatism, and other tectonism postdating continental fragmentation. *Reviews of Geophysics*, *16*(4), 621–688.

Thomas, M. Y., Lapusta, N., Noda, H., & Avouac, J.-P. (2014). Quasi-dynamic versus fully dynamic simulations of earthquakes and aseismic slip with and without enhanced coseismic weakening. *J. Geophys. Res.*, *119*, 1986–2004.

Toth, J., & Gurnis, M. (1998). Dynamics of subduction initiation at pre-existing fault zones. *J. Geophys. Res.*, *103*, 18053–18067.

Townend, J., & Zoback, M. (2000). How faulting keeps the crust strong. *Geology*, *28*, 399–402.

Twiss, R., & Moores, E. (1992). *Structural geology.* New York, NY: W.H. Freeman.

Tymofyeyeva, E., & Fialko, Y. (2015). Mitigation of atmospheric phase delays in InSAR data, with application to the Eastern California Shear Zone. *J. Geophys. Res.*, *120*, 5952–5963.

Walsh, J., & Watterson, J. (1988). Dips of normal faults in British Coal Measures and other sedimentary sequences. *Journal of the Geological Society*, *145*(5), 859–873.

Wang, K., & Fialko, Y. (2018). Observations and modeling of co- and postseismic deformation due to the 2015 M_w 7.8 Gorkha (Nepal) earthquake. *J. Geophys. Res.*, *123*(1), 761–779.

Weingarten, M., Ge, S., Godt, J. W., Bekins, B. A., & Rubinstein, J. L. (2015). High-rate injection is associated with the increase in US mid-continent seismicity. *Science*, *348*, 1336–1340.

Wernicke, B. (1995). Low-angle normal faults and seismicity: A review. *J. Geophys. Res.*, *100*, 20159–20174.

Wessel, P., Smith, W. H. F., Scharroo, R., Luis, J., & Wobbe, F. (2013). Generic Mapping Tools: Improved Version Released. *Eos, Trans. AGU*, *94*, 409–410.

Yang, W., & Hauksson, E. (2013). The tectonic crustal stress field and style of faulting along the Pacific North America Plate boundary in Southern California. *Geophys. J. Int.*, *194*, 100–117.

Yang, W., Hauksson, E., & Shearer, P. M. (2012). Computing a large refined catalog of focal mechanisms for southern California (1981–2010): Temporal stability of

the style of faulting. *Bull. Seism. Soc. Am.*, *102*, 1179–1194.

Zoback, M., Apel, R., Baumgartner, J., Brudy, M., Emmermann, R., Engeser, B., . . .
    Vernik, L. (1993). Upper-crustal strength inferred from stress measurements to
    6 km depth in the KTB borehole. *Nature*, *365*, 633–635.

Supporting Information for "Estimation of absolute stress in the hypocentral region of the 2019 Ridgecrest, California, earthquakes"

Y. Fialko[1]

[1]Institute of Geophysics and Planetary Physics, Scripps Institution of Oceanography, University of California, San Diego, La Jolla,

California, USA.

Contents of this file

May 8, 2021, 8:12pm
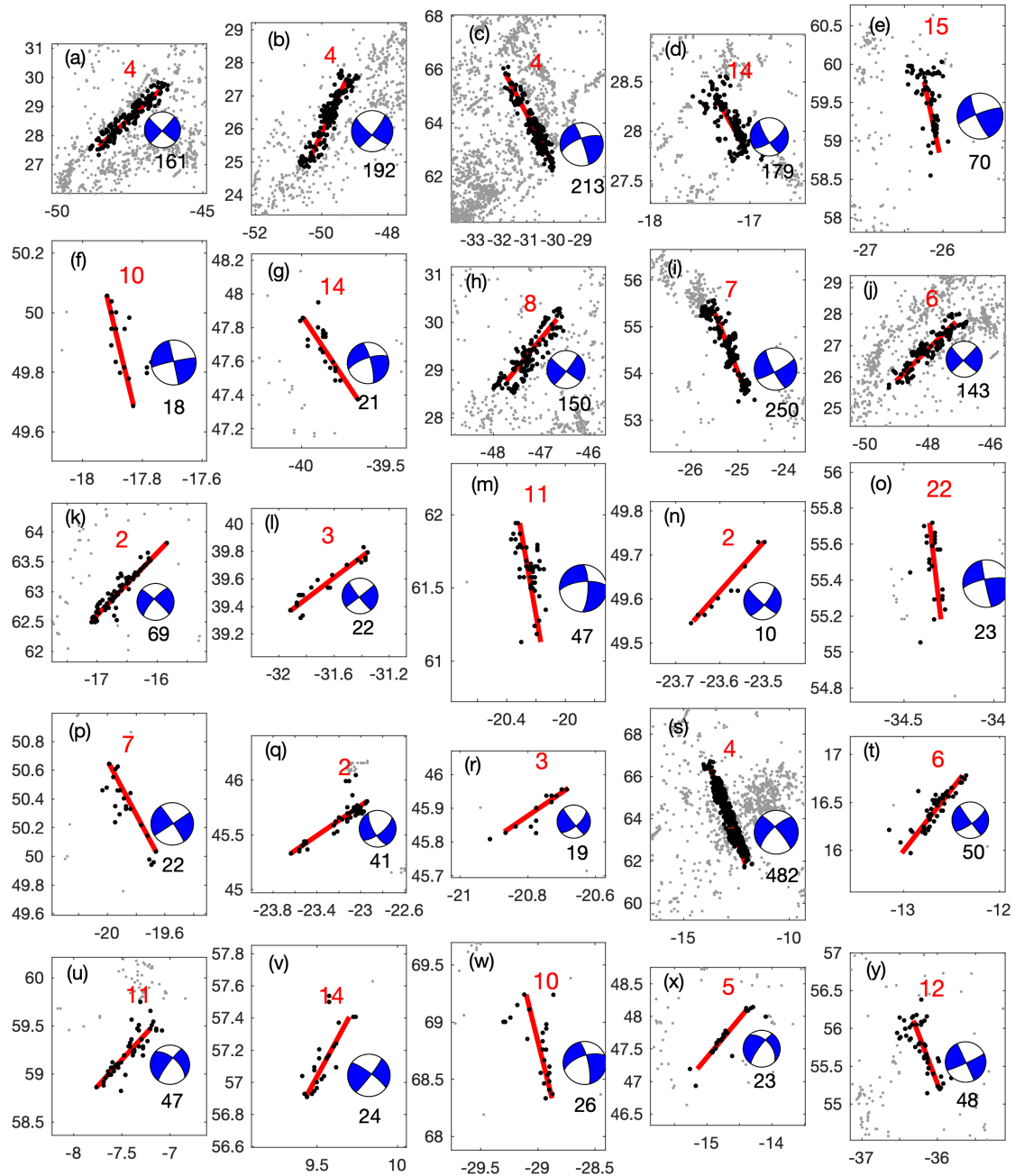
Figure S1: Seismicity lineations identified by the clustering algorithm. Grey dots denote the background seismicity, black dots denote events included in a cluster. The local UTM coordinate system is the same as in Figure 1 in the main text. Red lines denote the best linear fits. White and blue "beach balls" denote the composite focal mechanisms for the respective clusters. Black numerical labels below the beach balls indicate the number of events in a cluster. Red numerical labels above the beach balls indicate uncertainty in the estimated strike angle, in degrees.

May 8, 2021, 8:12pm
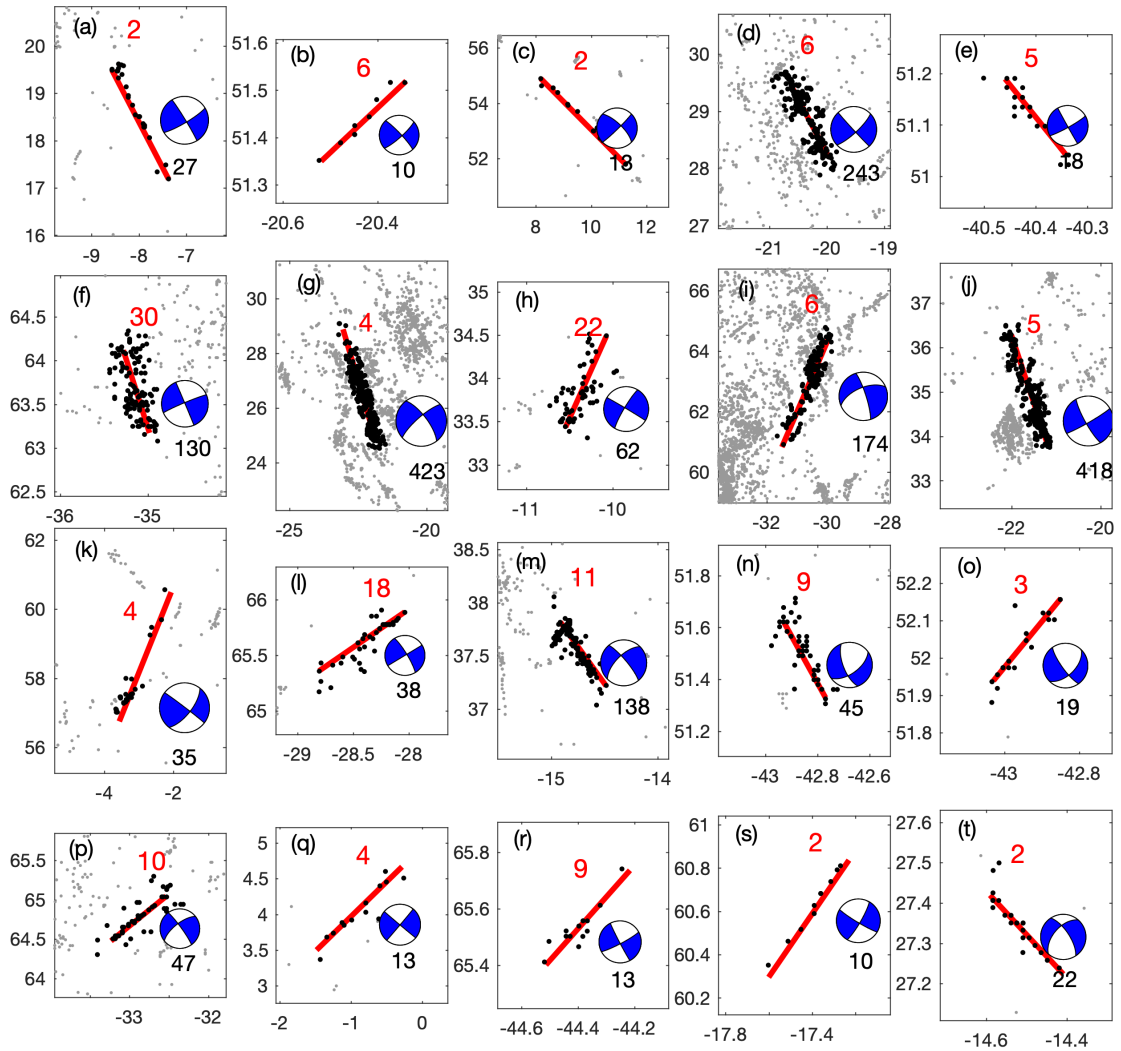
Figure S2: Seismicity lineations identified by the clustering algorithm. Notation is the same as in Figure S1.

May 8, 2021, 8:12pm
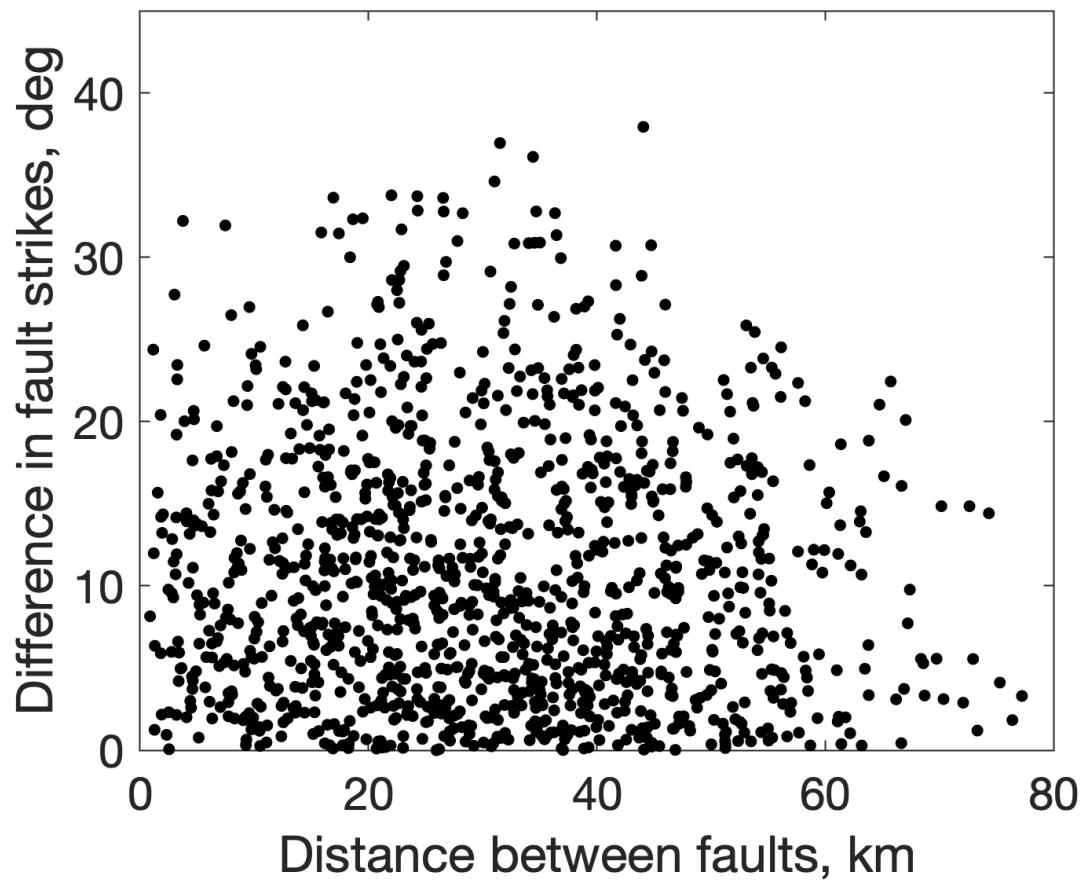
Figure S3: Variability in fault strikes for faults having the same sense of slip, as a function of distance between the faults.
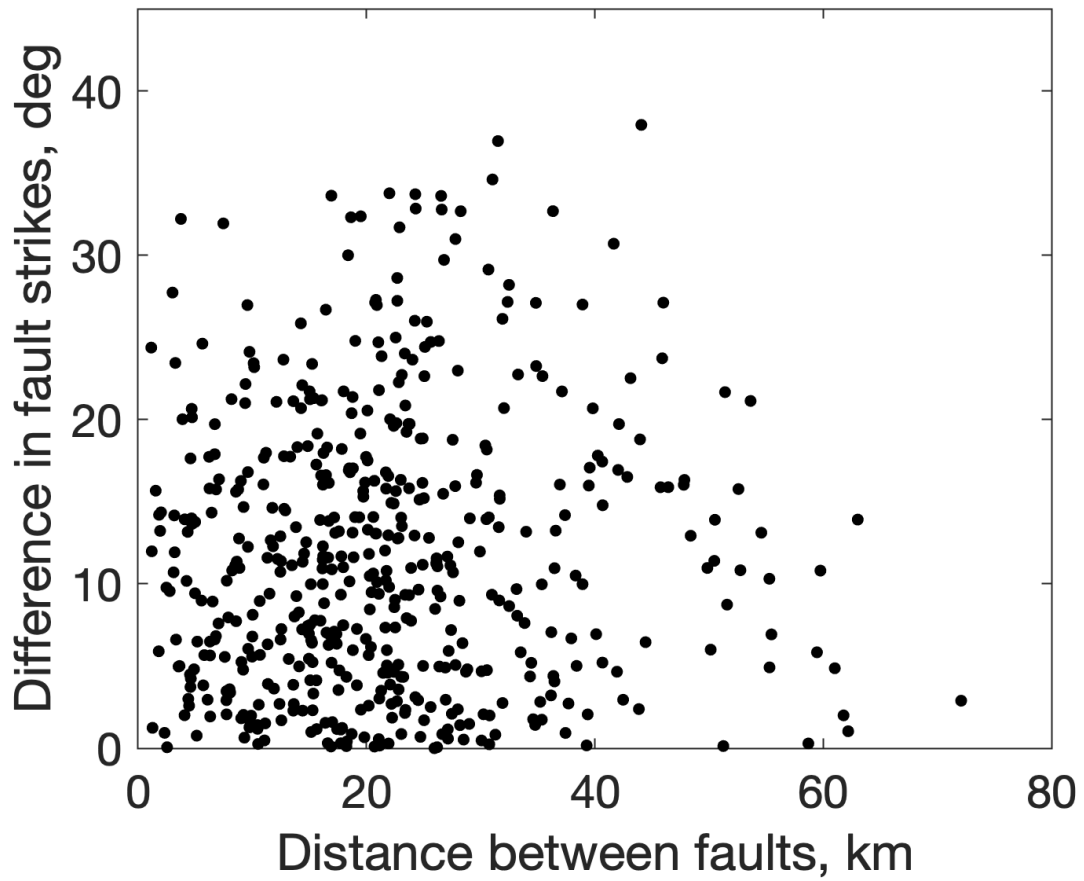
Figure S4: Same as Figure S3, for events with northings > 40 km (see Figure 3 in the main text).
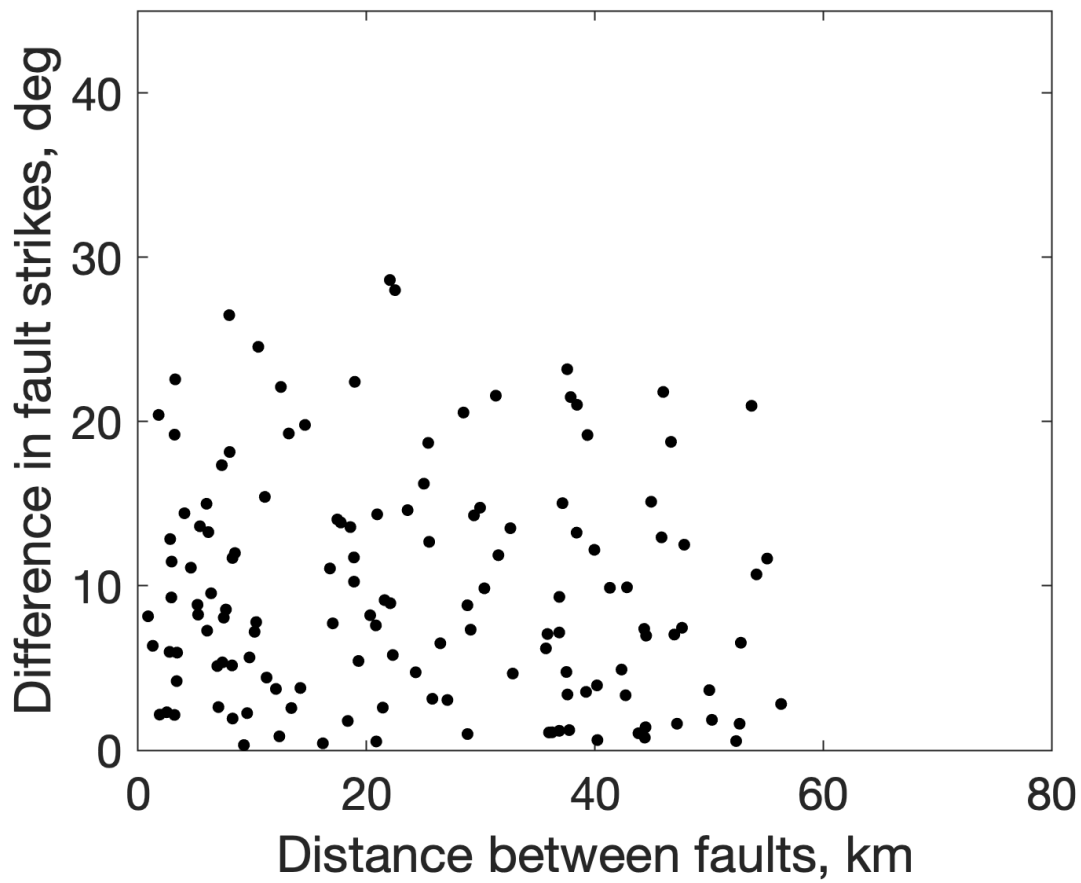
:

Figure S5: Same as in Figure S3, for events with northings < 40 km (see Figure 3 in the main text).
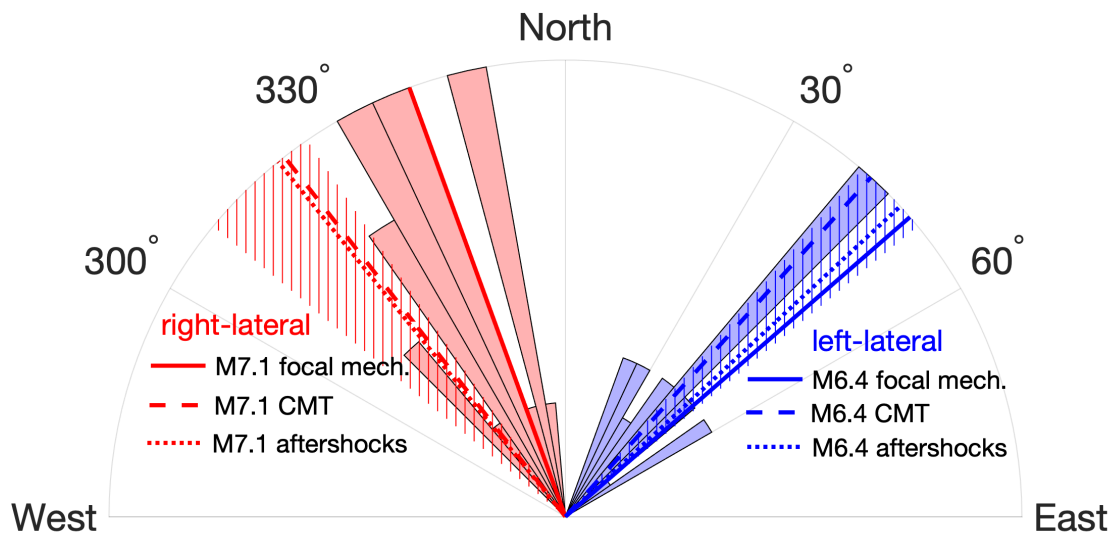
Figure S6: Distribution of strikes for a subset of faults with northings > 40 km (see Figure 3 in the main text). Notation is the same as in Figure 4 in the main text.
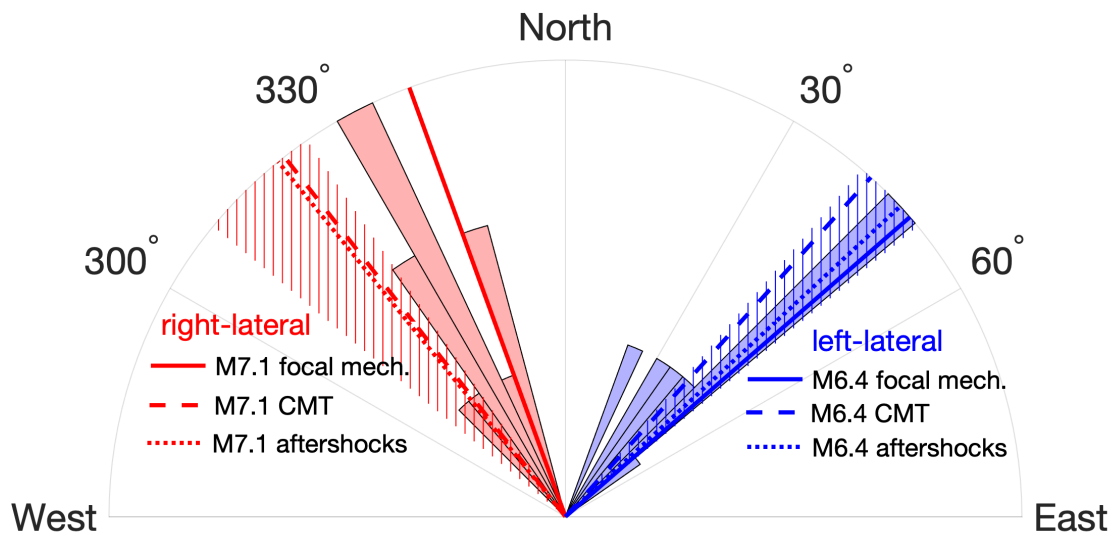
Figure S7: Distribution of strikes for a subset of faults with northings < 40 km (see Figure 3 in the main text). Notation is the same as in Figure 4 in the main text.